APS physics

CHORUS

This is the accepted manuscript made available via CHORUS. The article has been published as:

High-Contrast Material Identification by Energetic Multiparticle Spectroscopic Transmission Radiography

J. Nattress, T. Nolan, S. McGuinness, P. Rose, A. Erickson, G. Peaslee, and I. Jovanovic

Phys. Rev. Applied **11**, 044085 — Published 26 April 2019

DOI: 10.1103/PhysRevApplied.11.044085

High-contrast Material Identification by Energetic Multi-particle Spectroscopic Transmission Radiography

J. Nattress[1],* T. Nolan[1], S. McGuinness[2], P. Rose[3],* A. Erickson[3], G. Peaslee[2], and I. Jovanovic[1†]
[1] *Department of Nuclear Engineering and Radiological Sciences, University of Michigan, Ann Arbor, MI 48109 USA*
[2] *Department of Physics, University of Notre Dame, Notre Dame, IN 46556 USA and*
[3] *G.W. Woodruff School of Mechanical Engineering, Nuclear and Radiological Engineering Program, Georgia Institute of Technology, Atlanta GA 30332, USA*
(Dated: April 1, 2019)

Transmission radiography using MeV-class radiation is a powerful non-destructive method for determining the elemental composition. Radiography is typically performed using either neutrons or photons, but neither of these probes is universally applicable. We experimentally demonstrate that a significant improvement in the contrast for small elemental variations in object composition can be realized by combining the multiple monoenergetic neutron and photon transmission radiography techniques. The multimodal source is based on deuteron-driven low-energy nuclear reactions that produces both neutrons and photons at discrete energies. The neutron time-of-flight technique was employed to measure the transmission over a broad range of neutron energies and was combined with spectroscopic photon transmission. This work demonstrates the use of a single, multi-particle, multiple monoenergetic radiation source and a single radiation detector type to simultaneously perform neutron and photon spectroscopic radiography. Four different material identification metrics are employed, which show a factor of three or higher increase in sensitivity to changes in material composition when compared to the traditional dual-energy photon radiography, and are in agreement with simulations that establish the direct correspondence to known photon and neutron interaction cross sections. Further, the ability to infer the presence of objects consisting of impure elements, layers of different elements, or non-natural isotope concentrations is demonstrated.

I. INTRODUCTION

Radiography is a powerful imaging technique that has found widespread use in applications such as medicine, security, and inspection of industrial processes. One of the primary objectives of radiography is to disambiguate the geometrical shape of an object or an arrangement of objects and to infer the thickness via the observed opacity. The geometric configuration alone often does not provide adequate information for the desired application [1, 2]. Such is the case, for example, in screening for illicit transport of nuclear materials or narcotics, where benign substances must be distinguished from genuine threats. In the instance of nuclear material identification, the ability to differentiate among high-atomic number (Z) materials could reduce scanning times of ocean-going cargo containers, an existing gap in the current United States nuclear detection architecture [3].

Dual-energy photon transmission radiography is a traditional non-destructive technique that can be used to increase the contrast in radiographic images and/or determine the concentration of a particular element [4]. Since the 1950s, dual-energy (or dichromatic) transmission radiography has been used in a wide range of applications such as improving the quality of mammograms, inspecting industrial products, and finding narcotics, explosives, weapons, and illicit nuclear materials [5, 6].

Many of the applications currently use bremsstrahlung X-ray sources, where the endpoint energies of the sources can be varied. The measurements made over two overlapping energy ranges are compared in such a way to qualitatively infer the effective Z of the material the X-rays traverse. However, such measurements are typically made in the integral (current) mode, which reduces the value of spectroscopic information that is contained in an individual photon's energy. Also, the lower-energy photons (well below the endpoint bremsstrahlung energy) exhibit poor penetration through dense objects and may significantly contribute to the imparted radiation dose and degrade the image quality [7, 8]. Multiple-monoenergetic photon sources offer an advantage over bremsstrahlung sources in that the issues that arise from beam hardening do not exist [1]. A well-characterized monochromatic-photon source permits the selection of specific energies which provide the most meaningful data for a given application. In dual-energy monoenergetic photon transmission radiography [9, 10], photons of two distinct energies are used to exploit the dependence of the mass attenuation coefficient on both the photon energy and the atomic number. It is desirable for the photon energies to be adequately separated to ensure that a different photon interaction mechanism (photoelectric effect, Compton scattering, or pair production) dominates at the two chosen energies, since the cross sections of these mechanisms scale differently with atomic number and thus provide the elemental contrast.

There has been an increased interest in expanding the capabilities of radiographic methods to determine an object's effective atomic number while not having the

* Present Address: Oak Ridge National Laboratory, Oak Ridge, TN
† ijov@umich.edu

knowledge of the material areal density [11]. Material identification can be enhanced by combining complementary information that can be obtained from photon and neutron transmission radiography. It would be especially convenient if the nature of the probe is such that it produces both photons and neutrons. Further reducing the complexity of the approach, one could employ a single type of detector capable of performing spectroscopic measurements for multiple particle types (neutrons and photons).

Here, we present a radiography technique based on the same principles as dual-energy monoenergetic photon radiography, but which can significantly improve upon its performance. The technique, henceforth referred to as multi-particle spectroscopic transmission radiography (MPSTR), merges the information obtained from spectroscopic fast-neutron and photon transmission, where the nature of both radiation probes is multiple-monoenergetic. The multiple spectroscopic MPSTR probe originates from the same nuclear reaction process and can accurately identify pure materials and detect mixtures of material. Further, this method has a potential for use in identification of specific organic substances occurring in explosives and narcotics, or in detection of the presence of shielded special nuclear material (SNM). We demonstrate that the use of dual-mode (combined neutron/gamma-ray attenuation) transmission radiography makes it possible to measure smaller changes in the elemental composition of objects compared to single-mode (pure gamma-ray attenuation) radiography, and show that the experimental results can be well predicted by simulations that employ the known photon and neutron interaction cross sections. We show that on a per-particle basis (whether for neutrons or photons), a more precise measurement of an unknown pure material is possible when combined neutron and gamma-ray radiography is performed as compared to single particle (gamma-ray) radiography. Finally, we demonstrate how the multiple metrics can be used to infer anomalies that imply the presence of elemental mixtures, non-natural isotopic concentration, or objects consisting of layers of different elements.

II. PRINCIPLES OF MULTI-PARTICLE SPECTROSCOPIC TRANSMISSION RADIOGRAPHY

The neutron/gamma-ray radiography source is based on nuclear reactions induced by few-MeV deuterons stopping in a boron-nitride (BN) target. The induced nuclear reactions produce multiple-monoenergetic, high-energy (>1 MeV) neutrons and gamma rays, which can be used to penetrate dense materials and perform spectroscopic radiography for material identification [12]. As the accelerated deuteron loses energy while stopping in the BN target, neutrons are produced at decreasing energies and are correlated to the excited states of the product nuclei and kinematics of the various reactions occurring in the target. Neutrons are continuously produced until the deuteron energy drops below both of the Coulomb thresholds of target nuclei – 1.7 MeV for ^{11}B. Table I lists the two main neutron-producing reactions from the deuteron-BN radiation source and the resulting gamma-ray energies [13, 14]

TABLE I: Major reactions occurring in deuteron-BN source with associated prominent gamma-ray energies [13, 14].

Reaction	Q-value (MeV)	Gamma-ray Energies (MeV)
^{11}B(d,nγ)^{12}C	13.73	4.44, 9.64, 15.1
^{14}N(d,nγ)^{15}O	5.07	5.18, 5.24, 6.18, 6.79, 7.28, 7.56

Recently, a similar source based on deuteron stopping in natural boron was used to perform material identification by dual-energy photon transmission radiography [9, 10, 15]. In this past work, atomic numbers of various objects and their areal densities were determined by spectroscopic photon radiography using two principal gamma rays produced in the reaction. While the accuracies within 5–10% when determining Z_{eff} were demonstrated, challenges remain when trying to distinguish among high-Z elements, such as SNM – uranium and plutonium – from non-SNM such as lead or tungsten [11]. The fundamental reason for this loss of contrast is the increased relative contribution of pair production in gamma-ray interactions with high-Z materials at lower gamma-ray energies. The dominant contribution of pair production mechanism at both higher and lower gamma-ray energies (4.4 and 15.1 MeV) used for spectroscopic radiography makes the gamma-ray cross-section scaling with Z nearly identical at two energies, reducing the performance of this method for Z-discrimination.

Several different photon and neutron sources have been suggested for use in a material identification MPSTR system [6]. Previously, MPSTR was implemented by combining a small, compact DT neutron generator with a radioisotope gamma-ray source [16]. The system was able to produce highly resolved radiographic images of air-freight containers. An MPSTR system using a DT neutron source in combination with continuous high-energy X-rays was explored, but no substantial work exists utilizing this specific combination [17, 18]. Another MPSTR system used a high-energy accelerator to accelerate deuterons into a gold or an aluminum target producing neutrons and photons [19]. In that work, a broad range of photon energies was measured with an endpoint energy close to 10 MeV. Neutrons at an approximate energy of 8.5 MeV were also produced. However, no robust material identification was reported. In Ref. [20], it was suggested that MPSTR could be used to detect SNM in cargo containers. In that work, deuterons were accelerated into a boron target to produce both neutrons

and photons. MPSTR was not pursued, nor was there an attemp to perform material discrimination using MPSTR. To date, no work has been reported using a single source to perform material identification using MPSTR. Further, no single type of detector has been used to simultaneously measure neutron- and photon- spectroscopic attenuation to support the material identification via MPSTR. Lastly, no work has been conducted that combines multiple spectroscopic MPSTR signals to perform material identification.

In a simple 1-dimensional case, interaction of a beam of monoenergetic photons with an absorber may be described as

$$I = I_0 \exp[-\mu_t x], \tag{1}$$

where I and I_0 are the intensities of the transmitted photons that did not undergo interactions, with and without the absorber present, respectively, μ_t is the total linear attenuation coefficient, and x is the absorber thickness. Interactions of a beam of monoenergetic neutrons with an absorber may be described similar to that for photons:

$$I = I_0 \exp[-\Sigma_t x], \tag{2}$$

where Σ_t is the total neutron macroscopic cross section of the absorber, while I and I_0 are the intensities of the non-interacting neutrons with and without the absorber present, respectively. A non-paraxial geometry, which can result from short source-to-object or object-to-detector distance, can limit the validity of the simple 1D attenuation model. In such cases, scattering can make a significant contribution to the detected radiation flux. While the scattering can be adequately modeled and accounted for, accurate estimation of the magnitude of this correction requires *a priori* knowledge of the composition and geometry of the scattering object. The following simplified analysis is therefore limited to the near-paraxial case.

Using the unique dependence of neutron interaction properties that depend on both the atomic and nucleon numbers, a quantity R indicating the material type can be defined that is directly correlated to energy-dependent neutron and photon cross-sections. Similar to dual-energy photon radiography, taking the ratio of μ_t in Eq. (1) and Σ in Eq. (2) eliminates the dependence of R on material mass and thickness:

$$R = \frac{\mu_t}{\Sigma_t} = \frac{\ln(I_{E_\gamma}/I_{E_\gamma,0})}{\ln(I_{E_n}/I_{E_n,0})} = \frac{\ln(T_{\gamma,E1})}{\ln(T_{n,E2})}. \tag{3}$$

Using Eq. (3), R-values corresponding to attenuation of monoenergetic photons and neutrons of given energies can be established. These R-values can then be experimentally determined by measuring the attenuation of two particle types at given energies. In the case of commonly-used bremsstrahlung radiation with varying endpoints, the aforementioned ratio may become sensitive to areal density [21]. In these cases, the ratio is no longer unique and is treated as a ratio of effective attenuation coefficients averaged over the bremsstrahlung spectra. The mass thickness is estimated from one of the bremsstrahlung spectra and a lookup table used to estimate Z [21].

III. MATERIALS AND METHODS

Experiments were conducted using the 10-MV FN tandem accelerator at the Institute for Structure and Nuclear Astrophysics (INSAP), University of Notre Dame. Neutrons and gamma rays produced from a 3-MeV deuteron incident onto a thick boron nitride (BN) target were measured with a 7.62-cm EJ-309 liquid scintillation detector [22] in two experimental configurations.

The detector was coupled to a 7.62-cm to 5.08-cm conical acrylic light guide and mounted to a Hamamatsu photomultiplier tube (PMT), model number R6321. The PMT was powered using a CAEN DT5533N desktop high-voltage power supply. The PMT anode signals were digitized using a CAEN DT5730 14-bit, 500-MS/s digitizer and saved to data files for post-processing. The digitizer was connected to a Linux-based computer via USB with a data transfer rate of 30 MB/s. The digitizer used the DPP PSD CAEN firmware package [23] and a `ROOT`-based graphical interface for data acquisition and display [24].

The objective sought in the first experimental configuration was to measure the neutron spectrum via the time-of-flight (TOF) technique. The detector was placed 7.3 m from the BN target, while a 1.3-m thick concrete wall separated the target from the detector. The detector was placed on beam axis, at a distance of ∼1.8 m from the floor and >4 m from the surrounding walls.

A 3-mm thick BN target, consisting of 95% boron nitride and 5% boron trioxide, was used to fully stop the 3-MeV deuterons. Due to the lack of a shielded neutron TOF tunnel at the INSAP facility, special considerations were made when designing the experiment. The BN target and the neutron TOF detector were placed in different rooms to provide a sufficiently long distance (∼8 m) for the TOF measurement. The two rooms were separated by a 1.3-m thick concrete wall, which collimated the neutron/gamma-ray source to an approximate beam diameter of 5 cm and reduced the abundance of room-scattered neutrons. The accelerator was operated to deliver a deuteron pulse every 600 ns (1 in 6 pulse selection from primary 10 MHz pulsed beam) with an approximately 17 nA of current on target. A beam buncher and sweeper reduced the duration of the deuteron pulse to <2 ns. Each accelerator pulse established a start signal, t_{start}, to mark the time the deuteron struck the BN target. The particle detector was fixed at measured distance, d, from the BN target. For each registered pulse in the detector, the threshold trigger time gave the time of detection, t_{stop}. The difference of $t_{start} - t_{stop}$, or the TOF, was tabulated.

The waveform data were processed to determine and subtract the waveform baseline and subsequently determine the pulse height, pulse-peak position, and the pulse-shape parameter (PSP), which allows the photon and neutron interactions to be identified. The PSP for an event is defined by charge integration:

$$PSP = Q_{tail}/Q_{full}, \tag{4}$$

where the total pulse area, Q_{full}, was calculated by integrating the waveform starting from 16 ns prior to the pulse peak for 200 ns, while Q_{tail} was calculated by integrating the waveform from 22 ns after the pulse-peak position to the end of the full integration bound.

Figure 1 shows the recorded event pulse shape and light output characteristics. The neutron and photon events are selected using a simple fiducial cut, where the events within the cut with a $PSP > 0.22$ are categorized as neutron interactions, while events within the lower cut centered at approximately 0.2 PSP are categorized as photon interactions.

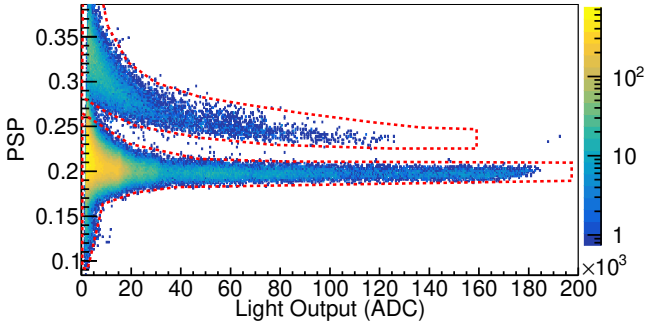

FIG. 1: Event characteristics recorded by the liquid scintillation detector with neutron and photon event selections shown (dotted red line).

The selected photons were used to determine the time when a deuteron strikes the BN target, which results in prompt gamma-ray emission. Figure 2 shows example recorded photon and neutron pulses and the corresponding accelerator pulses recorded during data acquisition. These prompt photons are produced from the deuteron striking the BN target and can be used to determine the time the deuteron strikes the target relative to the accelerator signal. Using this time correlation, the neutron TOF can be calculated. The width of the prompt gamma-ray peak is 5.85 ns, which results in a neutron energy resolution of ∼1 MeV at 14.5 MeV and ∼20 keV at 4 MeV. The TOF data for the selected neutron events was subsequently used to calculate the neutron energy spectrum.

The resulting spectrum is shown in Fig. 3, and is in good agreement with the spectra measured in similar experiments with the ^{11}B(d,nγ)^{12}C reaction [12, 20]. A significant broadening of the discrete neutron energy spectrum is observed, which is caused by the extended range

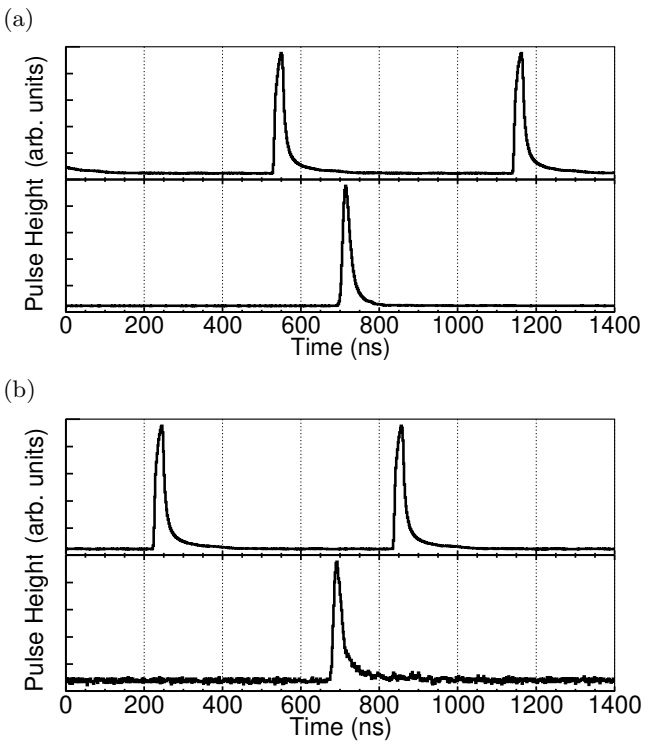

FIG. 2: (a) Accelerator signal (top) and corresponding photon event (bottom) and an (b) accelerator signal (top) and corresponding neutron event (bottom) recorded during data acquisition.

of deuteron energies during its stopping in the thick BN target.

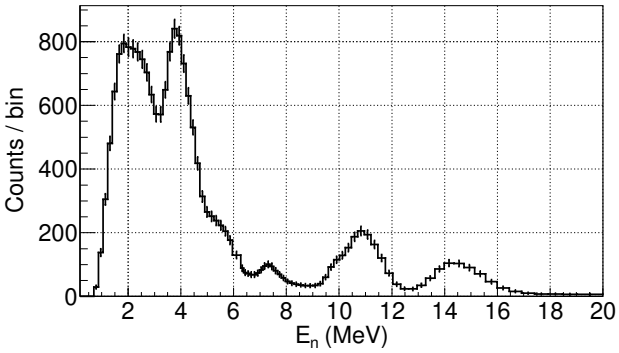

FIG. 3: Neutron energy spectrum reconstructed from the TOF measurement.

Five metallic test objects consisting of pure elements (Al, Cu, Sn, Pb, Bi) and one tungsten alloy test object (6% Ni, 4% Cu, and 90% W) were inserted into the beam path for transmission measurements; the particle transmission was measured for 120 minutes per object. All test objects consisted of elements in their natural isotopic abundance mix. The effective atomic number for the tungsten alloy was calculated using a custom open-

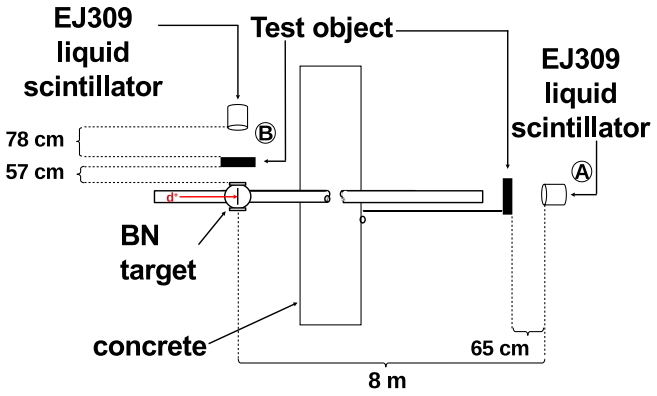

FIG. 4: Layout of the experiment: detector placement for Ⓐ the neutron TOF experiment and Ⓑ for the continuous-beam photon measurements.

source software, Auto-Z_{eff} [25]. Objects were placed one at a time at a distance of 60 cm from the face of the detector. Figure 4 illustrates the neutron TOF experimental configuration with an Ⓐ indicating the detector location. Table II lists the characteristics of objects used for the transmission measurements.

TABLE II: Properties of objects used in particle transmission experiments

Material	Z	Density (g cm^{-3})	Areal Density (g cm^{-2})
Al	13	2.7	18.1
Cu	29	8.96	17.1
Sn	50	7.3	25.1
W alloy	64.7	17	25.3
Pb	82	11.34	22.5
Bi	83	9.78	30.3

Monte Carlo simulations were performed in the `Geant4` framework [26] using the principal neutron energies produced (Fig. 3) in the d-BN reaction (4, 7.5, 11, and 14.5 MeV). The exact dimensions and compositions of test objects were modeled to study the effects of buildup in the detector, which correspond to the events that undergo scatter in the test object and subsequently interact in the detector. For each of the objects, 10^5 neutrons at each of four principal neutron energies were simulated; all neutrons whose which had their energy reduced by scattering and then deposited energy in the detector were tallied. The buildup effects were found to be negligible, as <1% of neutrons interacted with the detector.

As in the neutron TOF experiment, neutron and photon events were categorized based on their pulse shape. Due to the limited availability of experimental time, the experimental configuration was altered to achieve sufficient counting statistics when measuring the 15.1-MeV gamma rays from the d-BN source. In the second experimental configuration (marked as Ⓑ in Fig. 4), the detector and test objects were moved to the same room as the BN target, which shortened the detector-to-source distance and removed the concrete collimator. The detector was placed at an angle of approximately 90° with respect to beam axis, with the face of the detector 78 cm from the BN target, and the accelerator was operated in continuous mode for this measurement with approximately 160 nA of current on target. The objects were inserted between the BN target and the detector, and the particle transmission was measured for 30 minutes per object. The objects were placed so that they subtended the entire solid angle of the detector.

Figure 5 shows the measured light-output photon spectrum, with a distinct region due to 15-MeV gamma-ray interactions displayed in the inset. Other features are observable in the spectrum from other prominent gamma rays emitted by the source, but are more difficult to identify due to the modest detector energy resolution.

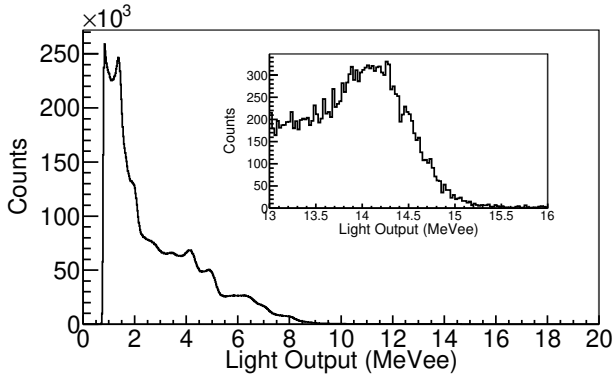

FIG. 5: Recorded unattenuated photon spectrum measured by the liquid scintillator

Simulation models for 15.1-MeV gamma-ray interaction with the liquid scintillator were previously developed and benchmarked with the measured light output spectra. The model is based on the `Geant4` toolkit and utilizes the standard EM physics package [26]. The detector resolution was characterized using the procedure outlined in Ref. [27].

A separate scintillation detector was used to monitor any accelerator beam-current fluctuations and normalize the individual object transmission measurements. The detector was located approximately 4 m from the BN target. Photon events located in the high-edge of the light output distribution – 10 MeVee to 15 MeVee – were selected, and the average detected photon rate was calculated. A normalization factor was calculated by dividing the measured photon rates observed during each of the objects experiments by the photon rate observed during the unattenuated source measurement. The calculation of the neutron and photon transmission used the unattenuated number of counts at each energy measured with the TOF detector increased by its corresponding normalization factor. This procedure was followed for both the pulsed- and continuous-beam experiments, with

continuous-beam experiment yielding similar results.

Due to the smaller target-to-object and object-to-detector distances in the continuous-beam experiment, gamma rays that undergo scattering could make a significant contribution to the recorded events in the detector. In order to fully understand the simulated detector response to 15.1-MeV gamma rays, a `Geant4` simulation was performed to study the buildup originating from 15.1-MeV gamma-ray interactions, while accounting for the dimensions and placement of each of the test objects. The simulation shows that a significant fraction of 15.1-MeV gamma rays undergo interactions that do not remove it or its secondary particle from the beam path. These scattered or secondary photons may interact with the detector and be detected, leading to departure from the simple one-dimensional Beer-Lambert attenuation model. Most scattered photons have energies well below 15.1 MeV and thus can make a contribution to the low end of the light output spectrum in the detector. The fraction of photons that undergo a reaction in the object but are still detected is approximately 10% for all objects used in the experiment. The gamma-ray transmission was corrected for small-angle scatter by scaling the total number of recorded 15.1-MeV events by the calculated buildup.

IV. RESULTS AND DISCUSSION

The transmission of 15.1-MeV gamma rays through the test objects was experimentally measured. The contribution of the 15.1-MeV gamma rays to the detector light output spectrum was determined in several steps. First, the measured background was subtracted from the light output distribution. Following the subtraction, the upper range of the distribution is solely the result of interactions of the highest energy gamma rays produced by the source, which is 15.1 MeV. Next, the simulated detector response to 15.1-MeV gamma rays was fit to the background-subtracted experimental light output spectrum. The total number of counts in the 15.1-MeV photon simulated-fit light-output distribution is the total number of 15.1-MeV photons detected.

Four prominent energies (4, 7.3, 11, and 14.5 MeV) were identified in the neutron energy spectrum. The neutron transmission at each of the four energies was measured by considering the counts under the peak and the neighboring energy bins (3.97–4.11, 7.18–7.45, 10.59–11.1, and 14.2–14.9 MeV).

Using Eq. (3), four R-values can be established, corresponding to the ratio of attenuation of neutrons at four different energies and 15.1-MeV gamma rays. The calculation of the predicted R-value assumes a natural isotopic abundance for materials that comprise the test objects. Figure 6 shows the experimentally measured R-values and their comparison to the calculated R-values for all naturally occurring elements.

From a measured R-value, the atomic number corresponding to the natural isotopic composition of an object can be calculated. Each of the calculated R-values is assumed to be normally (Gaussian) distributed, where the mean and standard deviation of each of the distributions is equal to the measured R-value and its respective standard deviation. Take, for example, the measured R_1 for the Al object. The Gaussian distribution for this R would have values of 0.362 and 0.08 for the mean and sigma, respectively. The calculated R-values are not continuous functions but are a series of discrete points.

To determine Z and its associated uncertainty from the discrete analytical R-values, Monte Carlo sampling is employed. A value is randomly sampled from the normal distribution of a single R. From the sampled value, the R-value is selected from the discrete analytical points in the distribution by selecting the value with the lowest residual. This Z-value is histogrammed.

The sampling is repeated N times ($N = 10^7$). From the newly sampled normal distribution in Z, the mean and uncertainty can be calculated. This Monte Carlo sampling is conducted for each of the four R-values and for each of the objects. A summary of the Z estimation for each of the R-values for all materials is provided in Table III; across all R-values agreement to the true Z was within 3σ of the expected value.

TABLE III: Estimation of element, denoted with its atomic number, for each $R_{n,\gamma}$.

Element	True Z	$Z(R_1)$	$Z(R_2)$	$Z(R_3)$	$Z(R_4)$
Al	13	12.8±4.0	17.4±5.8	11.9±3.2	14.7±3.2
Cu	29	27.3±1.2	26.8±4.5	28.6±2.9	30.1±6.0
Sn	50	53.7±3.2	52.3±2.4	54.0±1.7	55.8±3.0
W alloy	64.7	63.6±2.4	67.4±3.7	69.6±1.9	70.0±2.2
Pb	82	77.4±4.5	78.6±2.7	77.3±4.9	81.4 ±1.8
Bi	83	71.1±4.7	77.9±5.7	90.1±3.6	79.3±3.0

Single-mode gamma-ray radiography can also be performed using the d-BN source [9, 10, 15], which produces two prominent gamma-ray energies, 4.4 and 15.1 MeV. Interactions at these photon energies are dominated by different mechanisms, which scale differently with atomic number. At 4.4 MeV, the dominant interaction process is Compton scattering($\propto Z$), whereas pair production ($\propto Z^2$) is the dominant process for most elements at 15.1 MeV.

Figure 7 shows the energy-dependent variation of the total attenuation coefficient for uranium, lead, iron, and aluminum, which represent low- (Al), mid- (Fe), and high-Z (Pb and U) materials. The attenuation coefficients at 15.1 MeV are greater than at 4.4 MeV for the mid- and high-Z materials. These differences in attenuation allow the separation of high-Z from low- and mid-Z elements, but typically do not provide sufficient contrast to distinguish among high-Z elements.

For transmission measured at two distinct energies ($E1$

and $E2$), one can write

$$R = \frac{\mu_1}{\mu_2} = \frac{\ln(T_{E1})}{\ln(T_{E2})}. \quad (5)$$

Here, R is the ratio of the mass attenuation coefficients (or attenuation coefficients) at energies $E1$ and $E2$, which is unique to the element the photons traverse. Therefore, the ratio of the mass attenuation coefficients at two energies can be compared to the experimentally measured quantity $\ln(T_{E1})/\ln(T_{E2})$. If the analytically calculated ratio (R_γ) of attenuation of monoenergetic photons of 15.1 and 4.4 MeV are used as an example single-mode metric, the material discriminating power can be compared between single- and dual-particle metrics.

Figure 8 shows the calculated single-mode and dual-mode material determination R-values for all naturally occurring elements in the periodic table. The improved material discrimination capability of the $R_{n,\gamma}$-values when compared to the pure gamma-ray metric, R_γ, is qualitatively evident on Fig. 8. The variation between a range of elements can be described by the rate of change (the slope) of a line between two points. In our case, the higher the rate of change, the better the ability of the particular attenuation factor to distinguish between elements. The rate of change of the single-mode discriminant (attenuation of monoenergetic photons of 15.1 and 4.4 MeV) is a factor of three lower or more than all combined neutron/photon attenuation R-values. The power of the combined neutron/photon attenuation factors are further evident among high-Z elements ($74 \leq Z \leq 92$), where $R_{n,\gamma}$-values show an order of magnitude greater rate of change with Z compared to the pure gamma-ray metric, R_γ. The level of material discrimination in the high-Z range could enable discriminating between Pb and U, which would prove useful for many nuclear security and nonproliferation applications.

For practical applications such as cargo/luggage screening, often the object or objects being measured do not consist of a single pure element but are a mixture of different elements and thicknesses. For objects consisting of a single element with natural isotopic abundance, all experimentally measured R-values would reconstruct to the same atomic number Z. A deviation from consistency of this reconstruction would indicate that the object does not consist of a single element in natural isotope concentration, or that multiple layers of different elements are present in the beam path. Figure 9 presents the analytically calculated R-values and their corresponding Z values for two shielded object scenarios – uranium shielded with 10 cm of low-density polyethylene (LDPE) and uranium shielded with 10 cm of iron. The R values indeed do not reconstruct to identical Z for either of the shielded uranium objects. This inconsistency in Z-reconstruction for various R-values therefore successfully provides an indication that the object does not consist of a pure element in natural isotopic concentration, but is rather a mixture or multiple elements, includes non-natural isotope concentrations, or may be composed of mutliple layers of different elements.

This result could aid in anomaly detection and indicate information about possible shielding or a mixture of materials in the beam's path. By using multiple metrics – multiple R-values – these combinations of materials and shielding are readily discernible. As a natural extension of this method, it is possible to form hypotheses of the composition of materials and thicknesses of shielded objects and check for their consistency with multiple material discriminating factors (R) to arrive with the best interpretation.

The information gained on a per-particle basis can be compared between single-mode and dual-mode R-values. Monte Carlo simulations were performed in `Geant4` using the principal neutron (4, 7.5, 11, and 14.5 MeV) and gamma-ray energies (4.4 and 15.1 MeV) produced in the d-BN reaction and the dimensions of the aluminum, tin, and lead objects which represent a low-, mid, and high-Z object. At each of the discrete neutron and photon energies, 10^6 particles were directed in a beam with the exact size and shape of the respective object perpendicular to the object's face. The number of particles that traversed the target unimpeded were tallied. From these results, the five different R-values and their corresponding uncertainty in Z were calculated. Figure 10 shows the uncertainty in Z for each of the five R-values for aluminum, tin, and lead.

For each element, the dual-mode metrics outperform the single-mode metric and improves the precision of the reconstructed object's elemental composition. The optimal dual-mode metric changes as a function of Z, which should be considered when designing an experiment for a specific material or application. Depending on the elemental precision required, radiation sources and combinations of particles and energies could be specifically tailored for a given application. Although only three materials were analyzed, the greater elemental reconstruction power of the combined neutron/photon attenuation metric over the pure photon metric is evident.

V. CONCLUSIONS

A new transmission radiography technique that combines neutron and photon transmission was explored utilizing a d-BN source. It has been shown that, by using the experimentally measured transmission of two particle types, improved sensitivity to changes in elemental composition and a higher precision in elemental reconstruction is achieved as compared to a single-particle approach. Four preliminary metrics were developed based on neutron and photon transmission and show promise for improved material discrimination. Reconstruction of the elemental composition for various materials using combined neutron-photon transmission radiography yielded agreement with simulations that make use of known, tabulated cross section.

By measuring the neutron TOF, the incident neutron

energy spectrum can be determined. If the neutron light output distribution contains suitably distinct features, unfolding algorithms can be utilized to perform neutron spectroscopy without TOF. The EJ-309 detector may not be the ideal detector to use for neutron spectrum unfolding. Detectors that deliver more prominent features in their respective light output distributions such as deuterated liquids or solids [29–31] or capture-based detectors [32] could result in improved neutron spectrum deconvolution. By performing spectral unfolding to measure neutron energy, an accelerator used for this radiography technique could be operated in continuous mode. With a duty cycle near 100% and accelerator currents on order of mA (available from next-generation compact superconducting cyclotrons), significantly shorter experimental times could be achieved to yield equivalent material identification results.

ACKNOWLEDGMENTS

This work was supported by the U.S. Department of Homeland Security (2014-DN-077-ARI078-02 and 2015-DN-077-ARI096). The research of J.N. was performed under appointment to the Nuclear Nonproliferation International Safeguards Fellowship Program sponsored by the National Nuclear Security Administration's Office of International Safeguards (NA-241).

[1] C. Rizescu, C. Beşliu, and A. Jipa, Determination of local density and effective atomic number by the dual-energy computerized tomography method with the ^{192}Ir radioisotope, Nucl. Instrum. Methods in Physics Res., Sect. A **465**, 584 (2001).

[2] V. Ryzhikov, S. Naydenov, G. Onyshchenko, P. Lecoq, and C. Smith, A spectrometric approach in radiography for detection of materials by their effective atomic number, Nucl. Instrum. Methods in Physics Res., Sect. A **603**, 349 (2009).

[3] S. Martonosi, D. Ortiz, and H. Willis, 12. Evaluating the viability of 100 per cent container inspection at America's ports, The Economic Impacts of Terrorist Attacks **218** (2007).

[4] B. Jacobson, Dichromatic absorption radiography. Dichromography, Acta Radiologica **39**, 437 (1953).

[5] S. Kappadath and C. Shaw, Dual-energy digital mammography: Calibration and inverse-mapping techniques to estimate calcification thickness and glandular-tissue ratio, Med. Phys. **30**, 1110 (2003).

[6] Y. Liu, B. Sowerby, and J. Tickner, Comparison of neutron and high-energy X-ray dual-beam radiography for air cargo inspection, Appl. Radiat. Isot. **66**, 463 (2008).

[7] C. Geddes, B. Ludewigt, J. Valentine, B. Quiter, M.-A. Descalle, G. Warren, M. Kinlaw, S. Thompson, D. Chichester, C. Miller, *et al.*, Impact of Monoenergetic Photon Sources on Nonproliferation Applications Final Report, Tech. Rep. (Idaho National Lab.(INL), Idaho Falls, ID (United States), 2017).

[8] J. Jones, J. Sterbentz, W. Yoon, and D. Norman, in *AIP Conference Proceedings*, Vol. 1194 (AIP, 2009) pp. 43–48.

[9] P. Rose, A. Erickson, M. Mayer, J. Nattress, and I. Jovanovic, Uncovering special nuclear materials by low-energy nuclear reaction imaging, Sci. Rep. **6** (2016).

[10] B. Henderson, H. Lee, T. MacDonald, R. Nelson, and A. Danagoulian, Experimental demonstration of multiple monoenergetic gamma radiography for effective atomic number identification in cargo inspection, J. Appl. Phys. **123**, 164901 (2018).

[11] S. Naydenov, V. Ryzhikov, and C. Smith, Direct reconstruction of the effective atomic number of materials by the method of multi-energy radiography, Nucl. Instrum. Methods in Physics Res., Sect. B **215**, 552 (2004).

[12] T. Taddeucci, R. Sheffield, T. Massey, D. Carter, J. ODonnell, C. Brune, D. Ingram, D. Jacombs, and A. DiLullo, Neutron and gamma-ray production with low-energy beams, Los Alamos National Laboratories Report LA-UR-07-2724 (2007).

[13] J. Kelley, J. Purcell, and C. Sheu, Energy levels of light nuclei A = 12, TUNL Nuclear Data Evaluation Project (2019).

[14] F. Ajzenberg-Selove, Energy levels of light nuclei A = 15, TUNL Nuclear Data Evaluation Project (2019).

[15] B. O'Day III, Z. Hartwig, R. Lanza, and A. Danagoulian, Initial results from a multiple monoenergetic gamma radiography system for nuclear security, Nucl. Instrum. Methods Phys. Res., Sect. A **832**, 68 (2016).

[16] J. Eberhardt, S. Rainey, R. Stevens, B. Sowerby, and J. Tickner, Fast neutron radiography scanner for the detection of contraband in air cargo containers, Appl. Radiat. Isot. **63**, 179 (2005).

[17] K. Kang, H. Hu, Y. Xie, Q. Miao, Y. Yang, Y. Li, Z. Chen, and X. Wang, Method and equipment for discriminating materials by employing fast neutron and continuous spectral x-ray, (2008), US Patent 7,399,976.

[18] B. Sowerby and J. Tickner, Radiographic equipment, International Patent Application No, Tech. Rep. (PCT/AU03/01641, Filing date: 10 Dec, 2003).

[19] J. Rynes, J. Bendahan, T. Gozani, R. Loveman, J. Stevenson, and C. Bell, Gamma-ray and neutron radiography as part of a pulsed fast neutron analysis inspection system, Nucl. Instrum. Methods Phys. Res., Sect. A **422**, 895 (1999).

[20] M. Brandis, V. Dangendorf, C. Piel, D. Vartsky, B. Bromberger, D. Bar, E. Friedman, I. Mardor, I. Mor, K. Tittelmeier, *et al.*, in *AIP Conference Proceedings*, Vol. 1336 (AIP, 2011) pp. 711–716.

[21] S. Ogorodnikov and V. Petrunin, Processing of interlaced images in 4–10 MeV dual energy customs system for material recognition, Phys. Rev. Spec. Top. Accel Beams **5**, 104701 (2002).

[22] Eljen Technologies, Neutron/Gamma PSD Liquid Scintillator Data Sheet EJ-301, EJ-309, (Date Accessed: Apr 22, 2017).

[23] DPP PSD User Manual - UM2580, (2015), User's Manual for the DT 5730.

[24] Z. Hartwig, The ADAQ framework: An integrated toolkit for data acquisition and analysis with real and simulated radiation detectors, Nucl. Instrum. Methods Phys. Res., Sect. A **815**, 42 (2016).

[25] M. Taylor, R. Smith, F. Dossing, and R. Franich, Robust calculation of effective atomic numbers: The Auto-Z_{eff} software, Med. Phys. **39**, 1769 (2012).

[26] S. Agostinelli, J. Allison, K. a. Amako, J. Apostolakis, H. Araujo, P. Arce, M. Asai, D. Axen, S. Banerjee, G. Barrand, *et al.*, Geant4–a simulation toolkit, Nucl. Instrum. Methods Phys. Res., Sect. A **506**, 250 (2003).

[27] J. Nattress and I. Jovanovic, Response and calibration of organic scintillators for gamma-ray spectroscopy up to 15-MeV range, Nucl. Instrum. Methods Phys. Res., Sect. A **871**, 1 (2017).

[28] M. Berger and J. Hubbell, XCOM: Photon cross sections on a personal computer, Tech. Rep. (National Bureau of Standards, Washington, DC (USA). Center for Radiation, 1987).

[29] F. Becchetti, R. Raymond, R. Torres-Isea, A. Di Fulvio, S. Clarke, S. Pozzi, and M. Febbraro, Recent developments in deuterated scintillators for neutron measurements at low-energy accelerators, Nucl. Instrum. Methods Phys. Res., Sect. A (2017).

[30] M. Carman, A. Glenn, A. Mabe, F. Becchetti, S. Payne, and N. Zaitseva, Solution growth of a deuterated trans-stilbene crystal for fast neutron detection, J. Cryst. Growth **498**, 51 (2018).

[31] F. Becchetti, R. Torres-Isea, A. Di Fulvio, S. Pozzi, J. Nattress, I. Jovanovic, M. Febbraro, N. Zaitseva, and L. Carman, Deuterated stilbene (stilbene-d12): An improved detector for fast neutrons, Nucl. Instrum. Methods in Physics Res., Sect. A (2018).

[32] J. Nattress, M. Mayer, A. Foster, A. B. Meddeb, C. Trivelpiece, Z. Ounaies, and I. Jovanovic, Capture-gated spectroscopic measurements of monoenergetic neutrons with a composite scintillation detector, IEEE Trans. Nucl. Sci. **63**, 1227 (2016).

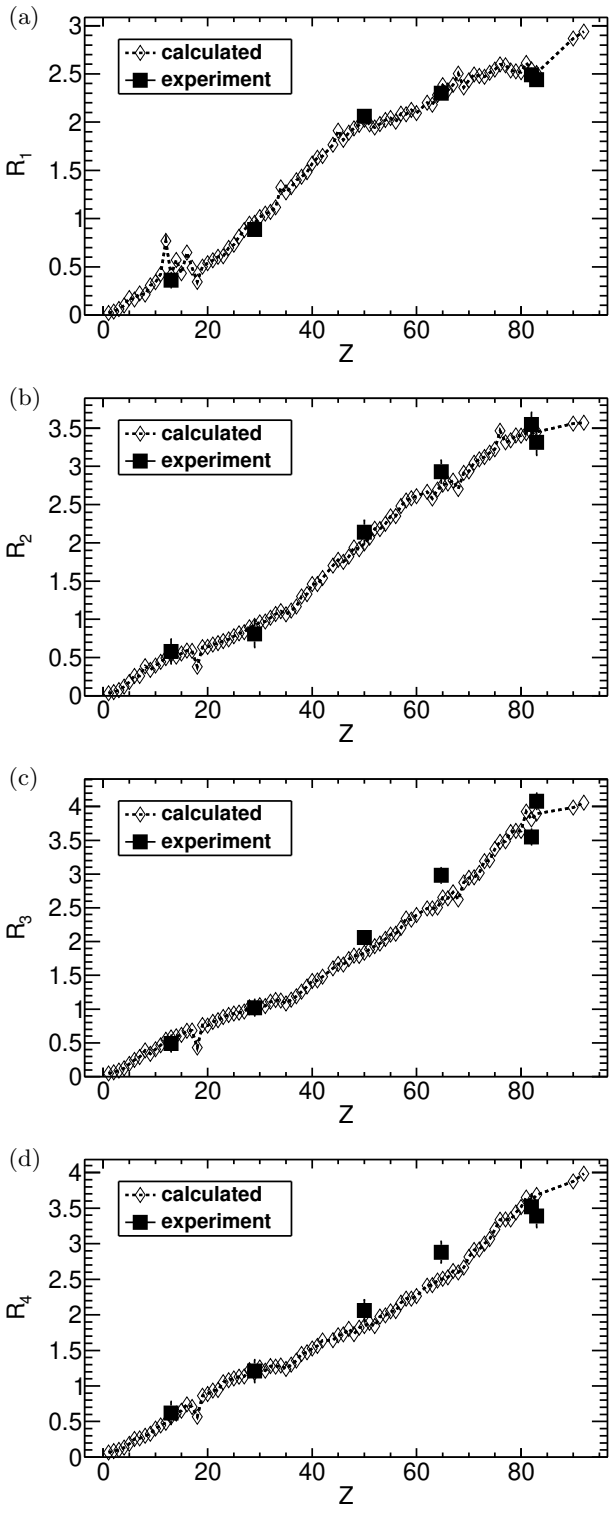

FIG. 6: The ratio of the natural log of the measured transmission (T) of 15.1 MeV photons to (a) 4 MeV neutrons(R_1), (b) 7 MeV neutrons(R_2), (c) 11 MeV neutrons(R_3), and (d)14 MeV neutrons(R_4) compared to the ratio of the mass-attenuation coefficient to the macroscopic cross section at those energies.

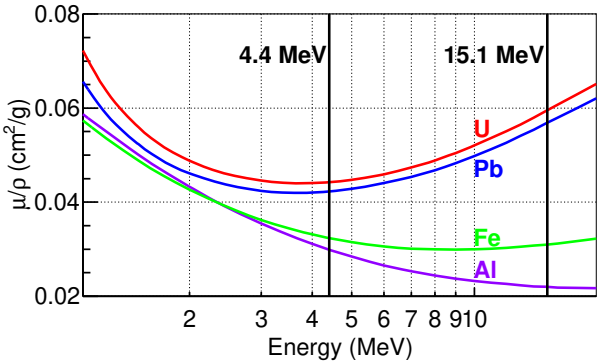

FIG. 7: Energy-dependent variation of the total attenuation coefficient for uranium (red), lead (blue), iron (green), and aluminum (purple) with two gamma-ray energies used for dual-energy transmission radiography [28].

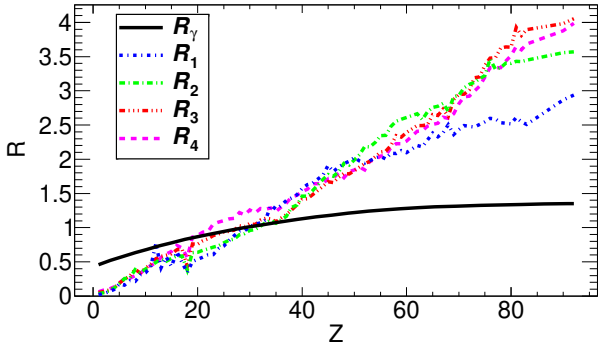

FIG. 8: Single-mode versus dual-mode R-values and the R-values.

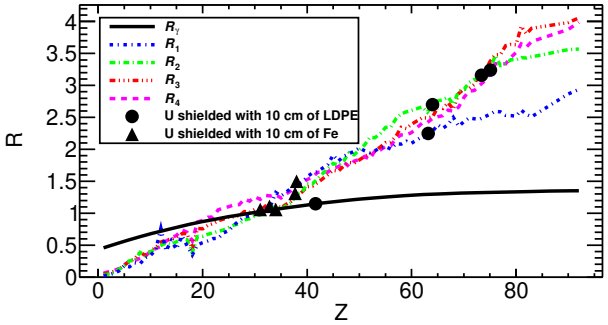

FIG. 9: Single-mode versus dual-mode R-values and the R-values calculated for two shielded scenarios (1) 1.1 cm of uranium shielded with 10 cm of LDPE and (2) 1.1 cm of uranium shielded with 10 cm of iron.

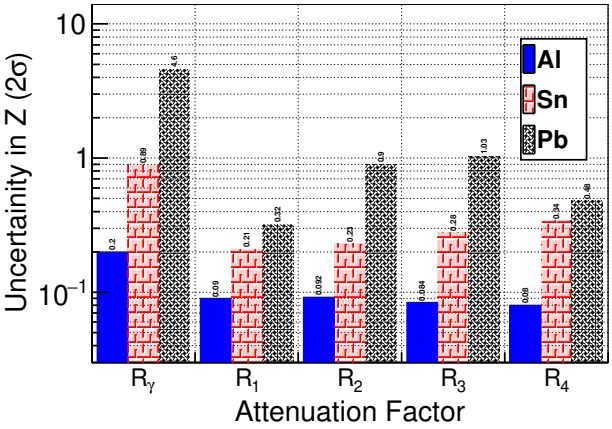

FIG. 10: Uncertainty in Z calculated from each of the five R-values for aluminum, tin, and lead using a fixed source particle number of source particles, N (N=10^6).